Cardiac Time Intervals Under Motion Using Bimodal Chest E-Tattoos and Multistage Processing

S. Bhattacharya, *Student Member, IEEE*, F. Santucci, *Student Member, IEEE*,
M. Jankovic, *Student Member, IEEE*, T. Huang, J. Basu, P. Tan, *Student Member, IEEE*,
E. Schena, *Senior Member, IEEE*, and N. Lu, *Senior Member, IEEE*

Abstract*—*Goal: **We present a wireless, lightweight, stretchable, and chest-conformable sensor, known as the chest e-tattoo, coupled with an advanced signal processing framework to accurately identify various cardiac events, and thereby extract cardiac time intervals (CTIs) even during body motion.** ***Methods:*** **We developed a wireless chest e-tattoo featuring synchronous electrocardiography (ECG) and seismocardiography (SCG), with SCG capturing chest vibrations to complement ECG. Motion artifacts often compromise the efficacy of SCG, but the e-tattoo's slim, stretchy design allows strategic placement near the xiphoid process for improved signal quality. Nine participants were monitored during walking and cycling. To accurately extract CTIs, we implemented a multistage signal processing framework, named the FAD framework, combining adaptive Normalized Least Mean Squares (NMLS) filtering, ensemble averaging, and Empirical Mode Decomposition (EMD).** ***Results:*** **Key CTIs, especially left ventricular ejection time (LVET), were successfully extracted by our hardware-software system and showed strong agreement with those reported by an FDA-cleared bedside monitor even during substantial movements. The pre-ejection period (PEP) measured by the e-tattoo also aligned with previous findings.** ***Conclusion:*** **The bimodal chest e-tattoo combined with the FAD framework enables reliable CTI measurements during various activities.** ***Significance:*** **Managing cardiovascular disease at home necessitates continuous monitoring, which has been challenging with wearables due to signal sensitivity to motion. Accurately extracting cardiac events from synchronous SCG and ECG during motion can significantly enhance heart stress response quantification, offering a more comprehensive cardiac health assessment than ECG alone and marking a significant advancement in ambulatory cardiovascular monitoring capabilities.**

***Index Terms*—Flexible electronics, wearable devices, cardiovascular monitoring, motion compensation, adaptive filter, empirical mode decomposition (EMD).**

I. INTRODUCTION

SEISMOCARDIOGRAPHY (SCG) captures the thoracic vibrations originating from cardiac contraction and the expulsion of blood from the ventricles into the vascular tree. These seismic vibrations generated by the heartbeat can be recorded on the chest surface using accelerometers, gyroscopes, fiber optic sensors, or piezoelectric films [1], [2], [3], [4], [5], [6]. The SCG signal was first discovered in 1964 [7] and gained popularity as a noninvasive technique for cardiovascular monitoring [8], [9], [10]. However, the reliance of the SCG on heavy equipment and its effectiveness contingent on how and where it is attached to the chest have made it eclipsed by the advent of advanced noninvasive imaging techniques, such as echocardiography, computed tomography (CT) and cardiovascular magnetic resonance imaging (C-MRI) [11].

Recent advancements in micro-electro-mechanical systems (MEMS) technology have revitalized interest in SCG monitoring. Modern MEMS accelerometers have made it possible to incorporate SCG monitoring into small, wearable devices, allowing for continuous and mobile heart monitoring [12]. This development overcomes the limitations of traditional imaging techniques, which typically require intermittent and stationary assessments.

The value of ambulatory cardiovascular monitoring is well recognized, driving the innovation of numerous medical devices over the years [13]. Devices like Holter monitors, which record ECG data for extended periods outside of clinical settings, have been essential. Although Holter monitors are effective in detecting various cardiac arrhythmias and intermittent abnormalities, they only capture the electrical aspect of heart functions, missing the mechanical dynamics.

SCG, in contrast, offers direct insights into the mechanical operation of the heart, providing information on blood flow,

Manuscript received 4 March 2024; revised 28 July 2024; accepted 25 August 2024. Date of publication 10 September 2024; date of current version 16 January 2025. This work was supported in part by the U.S. National Science Foundation (NSF) under Grant ASCENT-2133106, in part the U.S. Office of Naval Research (ONR) under Grant N00014-20-1-2112, in part by the U.S. Defense Health Agency STTR under Grant HT942523C0039, and in part by the UT-Austin Proof of Concept Award. *(S. Bhattacharya and F. Santucci contributed equally to this work.) (Corresponding author: N. Lu.)*

S. Bhattacharya, M. Jankovic, T. Huang, J. Basu, and P. Tan are with the University of Texas at Austin, USA.

F. Santucci is with the Unit of Automatic Control, Universitá Campus Bio-Medico di Roma, Italy, and also with the University of Texas at Austin, USA.

E. Schena is with the Unit of Measurements and Biomedical Instrumentation, Universitá Campus Bio-Medico di Roma, Italy.

N. Lu is with the University of Texas at Austin, Austin, TX 78712 USA (e-mail: nanshulu@utexas.edu).

This article has supplementary downloadable material available at https://doi.org/10.1109/TBME.2024.3454067, provided by the authors.

Digital Object Identifier 10.1109/TBME.2024.3454067

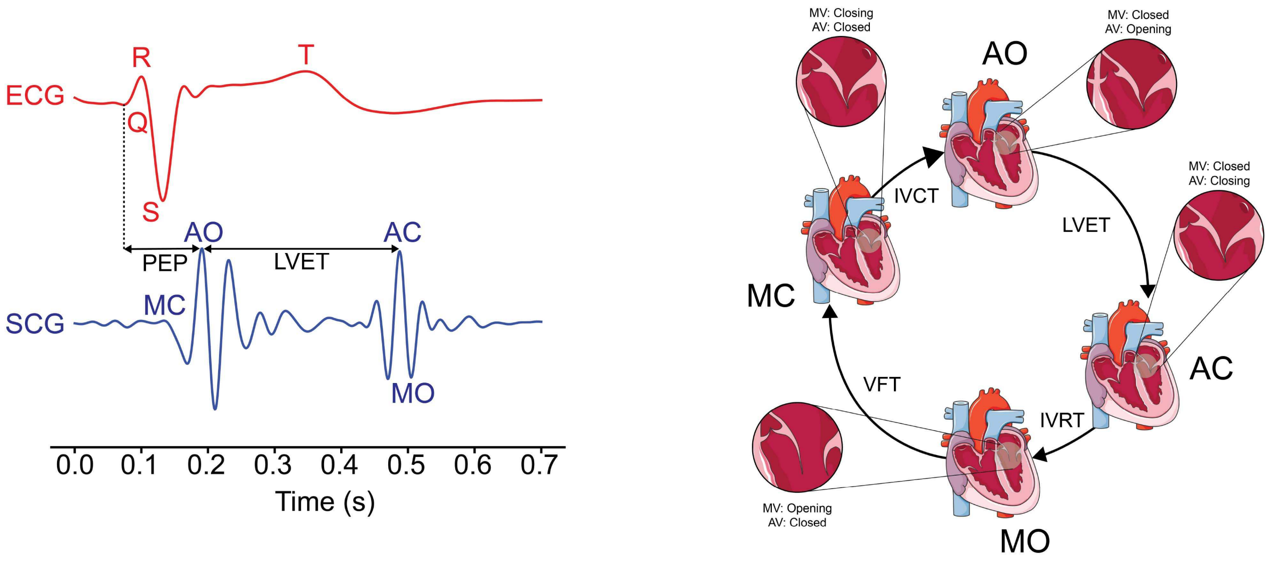

(a)

(b)

Fig. 1. (a) Synchronized electrocardiogram (ECG) and seismocardiogram (SCG) provide complementary information on cardiac activities, including the QRS complex and T-wave in ECG, and aortic valve opening (AO), aortic valve closing (AC), mitral valve closing (MC), and mitral valve opening (MO) in SCG. Pre-ejection period (PEP) is from the Q wave to the AO peak, and left ventricular ejection time (LVET) is from the AO peak to the AC peak. (b) Schematic illustrating different phases in the left ventricular heart cycle, highlighting the sequential opening and closing of the mitral valve (MV) and aortic valve (AV), as well as cardiac time intervals (CTIs) including iso-volumetric contraction time (IVCT), LVET, iso-volumetric relaxation time (IVRT), and ventricular filling time (VFT). The heart-chambers-visible icon by Servier (https://smart.servier.com/) is licensed under CC-BY 4.0 Unported https://creativecommons.org/licenses/by/4.0/ and has been modifed for this figure.

contractility of the heart muscle, valve activity, and other critical hemodynamic parameters such as stroke volume [14], [15], [16], [17]. Traditionally, clinicians have relied on phonocardiography (PCG) as the primary method to assess valve dynamics by listening to cardiac sounds [18], [19]. However, SCG, operating at lower frequencies (up to 40Hz) compared to PCG (up to 750Hz), offers a deeper understanding of cardiac mechanics, such as blood flow. In addition, SCG is less affected by ambient noise than auscultation, which makes it promising for continuous ambulatory monitoring.

Combining ECG and SCG monitoring in a single device allows for the simultaneous tracking of the heart's electrical and mechanical activities. This combined approach promises a deeper understanding of cardiovascular health in everyday settings.

The capability of the SCG in detecting the precise moments of cardiac valve movements has been proven [20], [21]. Fig. 1(a) displays synchronized ECG and SCG signals for a single heartbeat, with the key features clearly labeled. Fig. 1(b) shows diagrams that highlight important valve movements and their related timings within a cardiac cycle. The start of ventricular systole, indicated by the first peak in SCG right after the R peak in ECG, precisely captures the closure of the mitral valve (MC). It is immediately followed by the first major peak in the SCG, known as the aortic valve opening (AO) peak, which marks the beginning of the ejection period. The second major peak in the SCG records the aortic valve closing (AC), followed by the mitral valve opening (MO) peak, which signifies the start of diastole and the initiation of ventricular filling, respectively. The precise timing information enables the calculation of key cardiac time intervals (CTIs), such as the pre-ejection period (PEP) and the left ventricular ejection time (LVET), which are vital for assessing heart function [22]. For example, previous work has discovered their correlation with cardiac ejection fraction (EF) [23] and left ventricular failure [24], [25].

However, the development of wearable SCG sensors for everyday use has been hampered by motion artifacts. Motion sensors used to collect the SCG from the surface of the human chest inadvertently capture all body movements including respiration, not only heart valve actions, leading to considerable signal contamination. The issue of motion artifacts is evident when one notices that sternal vibrations due to the heartbeat induce accelerations typically between 5–10 milli-g (mg) ($1g = 9.8\,\mathrm{m/s^2}$), in contrast to activities of daily living such as walking, which can produce accelerations of several hundreds of mg (refer to Fig. S12 in supplementary material). Furthermore, the noise of motion artifacts overlaps with the frequencies of the SCG signal, which range from 1–40 Hz, depending on the phenomena being studied [3]. The primary heartbeat component is generally found within the 0.5–2 Hz range, while additional components and harmonics may reach higher frequencies. Frequencies associated with daily activities also fall within this low-frequency range [33], [34]. We illustrate this by performing the Fourier transform of SCG signals during different activities and observing their magnitudes (see Figs. S11C-E).

The considerable difference in magnitudes and the overlapping frequency bands cause difficulty in isolating and precisely interpreting SCG signals during movements. Addressing this

TABLE I
PRIOR STUDIES WHICH FOCUSED ON REMOVING MOTION ARTIFACTS FROM SCG SIGNALS DURING SUBJECT'S MOVEMENTS HAVE UTILIZED A VARIETY OF HARDWARE AND SOFTWARE APPROACHES

Reference	Sensor	No. of Sensors	No. of Subjects	Activities	Motion Compensation Framework	Parameters Estimated	Gold Standard
This work	ADXL355	1	9	Normal to brisk walking, cycling	FAD	HR, LVET, PEP	NICOM
[26]	LIS3L02AL	1	6	Normal pace walking	SG smoothing	HR	ECG
[27]	Shimmer 2	1	40	Walking slower than 1.3 m/s	NLMS AF	AO peaks, HR	ECG
[28]	Shimmer 3	2	10	Slow walking	NLMS AF	SCG beats	ECG
[29]	Shimmer 3	3	14	Walking and jogging	Constrained ICA	HR, PEP	ECG, ICG Biopac
[30]	9DoF	1	30	Body positions and running	SG filter	HR	ECG
[31]	ICM-20602	1	16	Low speed walking	RLS AF	AO, HR	ECG
[32]	BMA280	1	17	Normal and brisk walking	EMD	PEP	ECG, ICG Biopac

These methods include savitzky-golay (SG) filtering, normalized least mean square (NLMS) algorithms, adaptive filters (AF), recursive least square (RLS) techniques, and independent component analysis (ICA).

challenge is imperative for advancing the viability of ambulatory SCG monitoring in real-life scenarios.

Numerous studies have sought to overcome this challenge with varying levels of success, employing a range of signal filtering or decomposition techniques. Key insights from the most relevant prior works are summarized in Table I. These efforts have mainly focused on extracting cardiac sounds, heart rate (HR), or the AO peak (and consequently PEP). However, difficulties arise in restoring the SCG waveform to discern the AC peak, a necessity for accurate LVET extraction. The importance of LVET in cardiovascular assessment has been underscored in many studies, particularly in conditions such as mitral valve stenosis, arterial hypertension, and atrial fibrillation [35], [36], [37]. Therefore, despite the diversity of methods, continuous SCG denoising and comprehensive CTI extraction have not yet been achieved.

Our contributions in this work comprise a comprehensive hardware-software system that combines low-power and high-fidelity chest e-tattoo with sophisticated signal processing framework to achieve accurate CTI measurements during physical activities. The main components of the system are summarized as follows:

- An improved bimodal chest e-tattoo with light weight, mechanical flexibility, and body-conformal characteristics, which enable high quality physiological signal capture from an anatomically challenging region.
- A software framework that is validated in vivo to effectively eliminate motion artifacts from the SCG. This framework, named FAD (filter, averaging, empirical mode decomposition), allows for the extraction of LVET during various physical activities, a capability that, to the best of our knowledge, has not been previously achieved.

The effectiveness of this framework is evaluated by comparing the LVET data from the e-tattoo with that from an FDA-cleared impedance cardiogram (ICG) of nine participants performing various activities, such as walking at various speeds and cycling under varying loads. This comparison aims to validate the reliability and accuracy of the FAD framework in monitoring cardiac dynamics during body movements.

II. METHODS

A. Design and Application of the Dual-Mode E-Tattoo

The e-tattoo is a stretchable chest-laminated cardiovascular monitoring device, representing a modified version of the device introduced in our earlier research [38]. The e-tattoo features a flexible printed circuit (FPC) structured into islands interconnected with serpentine traces that enable stretchability [39](Fig. 2(a)). The islands serve as platforms for housing rigid elements, which include passive components and integrated circuits (IC), responsible for sensing, computing, and communication. Components designated for specific functions or sharing the same communication channel are segregated onto distinct islands, reducing the number of interconnections needed and thereby improving the overall robustness of the device. This design preserves the optimal electronic density and simplifies the manufacturing process. In addition, employing serpentine interconnections imparts stretchability to the device.

The e-tattoo, which is capable of synchronizing the measurement of ECG (MAX30003), SCG (ADXL355), and photoplethysmogram (PPG) (ADPD1080) signals, also intermittently measures skin temperature (TMP117). Each sensor is equipped with integrated analog front ends, which guarantees that solely digital data is communicated to the central processor. This design minimizes the susceptibility to noise from external factors, such as electromagnetic interference or body-coupled interference, ensuring accurate and reliable signal acquisition. To enhance signal fidelity, sensor measurements are synchronized using a peripheral-to-peripheral hardware synchronization scheme, effectively eliminating cross-modality timing errors. The central processing unit (nRF52832) is equipped with integrated

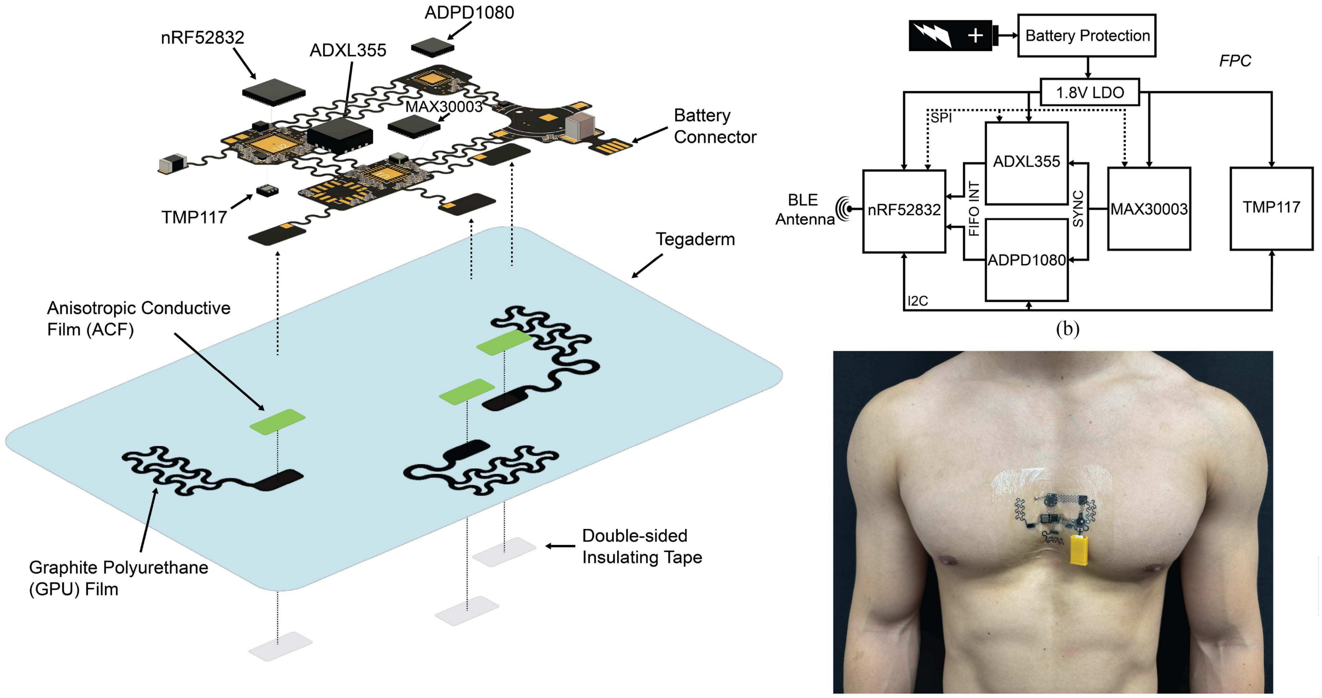

(a)

(b)

(c)

Fig. 2. (a) Different components of the wireless chest e-tattoo depicted in an exploded view. The two layers of flexible printed circuit (FPC) and graphite-polyurethane (GPU) electrodes on a Tegaderm tape are assembled to form the e-tattoo. (b) Circuit block diagram illustrating the primary hardware components of the e-tattoo and their interconnections. (c) A photo of the wireless, multimodal, chest-conformable e-tattoo.

Bluetooth Low Energy (BLE) capabilities, facilitating real-time transmission of data from the device to a designated receiver (Fig. 2(b)). In this case, an Android smartphone, paired with a custom designed application, enables real-time waveform display for monitoring device functionality. In addition, users can mark specific instances to timestamp significant events, aiding in post-processing analysis. The e-tattoo offers ultra-low power consumption when utilizing ECG and SCG only. The power consumption while actively transmitting data is 730 uA (see Fig. S19).

There are some distinct hardware modifications with regards to our previous work [38]. The SCG sensor has been shifted from the I2C line to the SPI line and has been physically placed next to the ECG sensor. This decision was made primarily because using I2C with this specific component led to communication instability, and switching to SPI communication provided additional power savings. Now that the SCG sensor is placed on the lower part of the e-tattoo, it can be placed closer to the xiphoid process more easily for better signal quality. Another modification is the inclusion of a low-resolution accelerometer (MC3635) to measure whole-body motion. It is not sensitive enough to measure SCG but can detect motion and body orientation. Lastly, a power connector flap was added to the FPC design. This enables a lithium polymer (LiPo) battery to be easily clipped or swapped to supply more power than a coin cell battery used previously.

The ECG sensor requires robust electrical contact with the skin, achieved using dry electrodes made from graphite polyurethane (GPU) film cut into custom patterns by precision laser cutting and transferred onto a medical dressing (Tegaderm, 3M). The detailed process is explained in supplementary materials Section I. Dry electrodes offer advantages over gel electrodes, such as immunity to signal degradation due to electrode dehydration [40], [41] and a slim form factor. To establish electrical connections between layers, holes are punctured through the Tegaderm, and z-axis anisotropic conductive film (ACF) links the FPC layer with the dry electrodes (Fig. 2(a)). This assembly technique enables a temporary linkage between the device and the electrodes, which simplifies the disposal of electrodes after use and the recycling of electronic components. In this configuration, only the medical dressing and the biocompatible GPU make direct contact with the skin, ensuring electronic isolation. This design prioritizes user comfort, device reusability, and long-term functionality.

The device is laminated on the chest near the lower sternum, such that the ECG electrodes span across the sternum to provide a strong signal with a sharp R peak (Fig. 2(c)) and the SCG sensor is in close proximity to the xiphoid process. Within the realm of SCG, an ongoing challenge revolves around determining the optimal position for signal measurement. Currently, there is no standardized protocol for sensor placement for SCG recording. The significance of sensor positioning comes from well-established evidence indicating that the SCG morphology undergoes changes based on the location of the sensor on the chest surface. [42], [43], [44], [45], [46]. Previous studies have attempted to document these changes in the waveform and identify locations on the anterior chest that consistently guarantee high repeatability in measurement, signal strength, and a high signal-to-noise ratio [5], [43], [44], [47]. Furthermore, it has

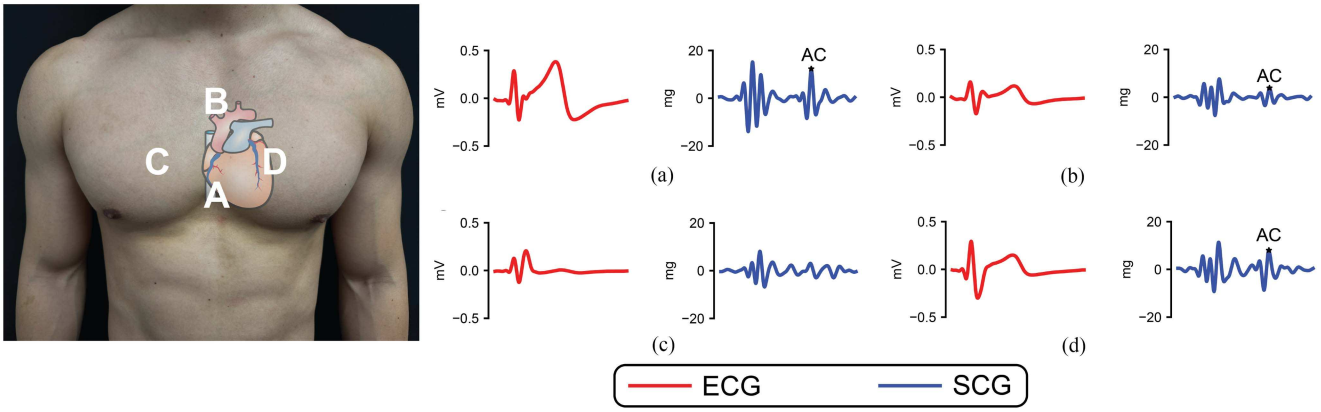

Fig. 3. Comparison of electrocardiogram (ECG) and seismocardiogram (SCG) captured by the e-tattoo attached at various chest locations. Position A, the xiphoid process, exhibits an SCG of greater amplitude, featuring more pronounced first and second heart vibrations, alongside a sharp ECG signal. In Position B, both signals appear significantly dampened, with the AC peak, required for LVET extraction, being notably subdued. The signal in Position C is rendered unusable due to substantial attenuation, likely attributed to its greater distance from the heart. Position D, situated on the left side of the thorax adjacent to the heart, manifest an SCG signal of reduced amplitude with the first and second vibrations discernible although attenuated.

been observed that the placement of the sensor can either subdue or amplify certain diagnostically significant features, such as the AC peak, thus affecting the feasibility of extracting clinically relevant parameters such as LVET [42], [48]. Previous studies have also highlighted how variations in SCG morphology are influenced by muscle mass and tissue properties of the thorax. Areas such as the xiphoid process are ideal for acquiring high-quality SCG signals due to their minimal fat content and bony underlying support.

However, in several previous studies using wearable SCG sensing systems during motion, applying the sensor near the xiphoid process was not entirely feasible due to the size, bulkiness, and rigidity of the hardware, leading to difficulties in conforming to the significant curvature of the sternal crest. Research studies utilizing such devices near the xiphoid have typically required the use of harnesses or belt-like apparatuses to secure the device in place [27], [30]. In contrast, many other investigations have chosen to place the sensor in the upper sternal region, closer to the suprasternal notch [32]. However, this location has been considered suboptimal for SCG detection, as previously highlighted and confirmed through our own tests (Fig. 3). Our thin, flexible, and stretchable device presents a distinctive advantage in enabling application at the optimal position without concerns of delamination or compromise of user comfort. This design choice addresses the limitations associated with traditional rigid systems, allowing optimal SCG sensing in a challenging anatomical region.

B. Motion Compensation Technique

The FAD framework leverages the implementation of adaptive filters, ensemble averaging, and EMD techniques in a sequential stack for motion compensation. For the sake of clarity, we will briefly delve into the fundamentals of these techniques.

1) Adaptive Filter: Adaptive filters, characterized by their dynamic parameter modification in response to evolving input signal characteristics, are particularly valuable in scenarios where signal properties fluctuate. These filters continuously adapt their coefficients to minimize the discrepancy between the actual and desired outputs, thereby effectively tracking and responding to changes in the input signal. Among various adaptive filters, the Recursive Least Squares (RLS) and Least Mean Squares (LMS) filters have shown promise in previous research focused on motion compensation for SCG signals [27], [28].

The LMS Algorithm stands out for its straightforward application and minimal computational demands, making it ideal for real-time scenarios. However, using a gradient-based method for updating weights, the LMS algorithm does exhibit a slower rate of convergence and a propensity for higher steady-state errors relative to the unknown system.

In the realm of noise and motion artifact mitigation, the Normalized Least Mean Squares (NLMS) filter excels at eliminating extraneous disturbances while retaining critical signal elements. This capability is particularly crucial in contexts where input signals are subject to frequent and dynamic variations, as observed in noise and motion compensation within biomedical signal processing [49], [50].

2) Empirical Mode Decomposition: The Empirical Mode Decomposition (EMD) method, recognized for significantly enhancing the signal-to-noise ratio in wearable SCG signals, represents an effective denoising strategy [32]. Developed by Huang et al., EMD is an adaptive technique tailored for analyzing non-stationary signals [51], [52], [53], [54]. It decomposes a signal into unique components called intrinsic mode functions (IMF), each representing distinct amplitude and frequency modulated tones inherent to the signal.

This decomposition is especially beneficial for SCG signal extraction during motion, as SCG signals are nonlinear and influenced by various physiological and external factors. EMD's adaptability, not requiring a predetermined basis like Fourier or wavelet transforms, is crucial for managing the unpredictable aspects of motion-corrupted SCG signals.

In addition, EMD aids in reducing noise from SCG signals. Identifying and removing IMFs that correspond to noise or artifacts, typically associated with higher frequencies or irregular

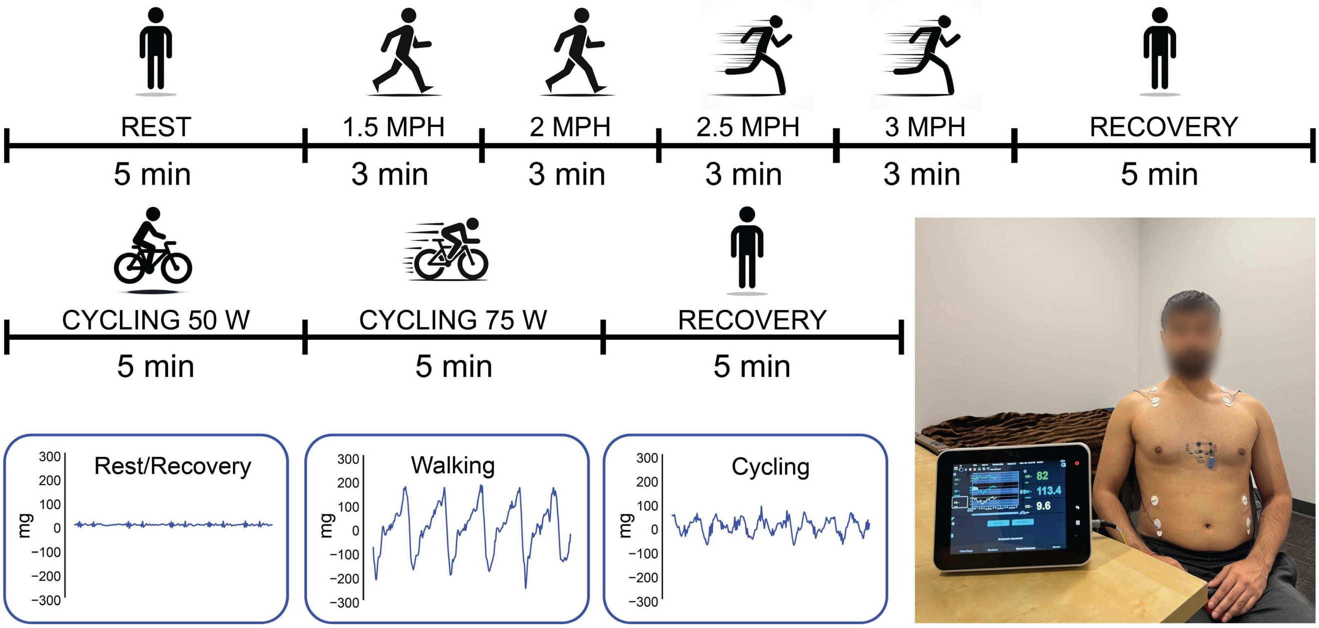

Fig. 4. Experimental protocol and setup. Three representative seismocardiogram (SCG) signals obtained during distinct activities (i.e., resting, walking, and cycling) are displayed to show the notable differences.

patterns [55] the process preserves cardiac core information in the SCG signal, thus enhancing its clarity.

III. Experimental Validation

A. Experimental Setup and Protocol

A study was carried out with 9 healthy volunteers (all male, age: 26.5 ± 4.1 years, weight: 150.7 ± 18.8 lbs, height: 69.5 ± 2.1 inches, and BMI 21.83 ± 2.23), following a protocol approved by the Institutional Review Board (IRB) at the University of Texas at Austin (IRB ID: STUDY00002313-MOD01). Informed consent was obtained from each participant prior to the beginning of the experimental session. Although no female participant joined the final trial, we have successfully conducted a pilot study on a female subject, and the results are given in Fig. S13, which shows the promise of our system on the female anatomy. More female participants will be recruited in an upcoming study in which trimodal e-tattoos with added photoplethysmography (PPG) capabilities will be tested.

The experimental protocol, illustrated in Fig. 4, included a sequence of activities: 5 minutes of rest, followed by 3 minutes of walking at 1.5 mph, 2 mph, 2.5 mph, and 3 mph. After a 5-minute recovery period, participants completed a 10-minute cycling session divided into two phases with incremental load, during which participants were asked to maintain a steady power output at 50 W and 75W. Some participants underwent an additional walking session at 4 mph for 3 minutes, where 4 mph was identified as the threshold speed at which the framework showed signs of failure (Supplementary Materials Fig. S2). This speed limitation is acceptable, as the study surpasses speeds used in the previous literature and already corresponds to a mild jogging phase at 4 mph.

Throughout the course of the study, participants simultaneously wore our e-tattoo and a noninvasive cardiac output monitor (NICOM), the Starling Fluid Management Monitoring System (Baxter International). The NICOM was utilized to measure various hemodynamic parameters, including HR and LVET, and these metrics were compared with data from the e-tattoo. The NICOM utilizes impedance cardiography (ICG) and was chosen as the gold standard for CTIs since it is noninvasive and FDA-cleared patient monitor. It also has the advantage of being semi-mobile as it can run on a battery for a short period of time.

In the raw SCG signals, an evident elevation in amplitude was observed during walking and cycling, in contrast to the signals obtained during the rest or recovery periods due to the introduction of motion artifacts. Fig. 4 illustrates this in a 3-second dorsoventral signal captured in three different phases of the protocol (rest / recovery, walking, and cycling) for the same participant. It is interesting to note that the amplitude variation observed during cycling was significantly lower in magnitude compared to that during walking.

B. Data Acquisition and Pre-Processing

The signals from the NICOM and the wearable e-tattoo sensors were synchronized by initiating them simultaneously. To confirm accurate alignment, the signals were subjected to a manual review, with time-axis data providing additional verification. For the analyses, only the dorsoventral SCG signal, corresponding to the z-axis component, was utilized.

In the signal preprocessing phase, the raw SCG signal is filtered through a tenth-order Butterworth bandpass filter with a cutoff frequency ranging from 1 to 40 Hz to extract the relevant SCG signal. The raw signal is also processed using a bandpass

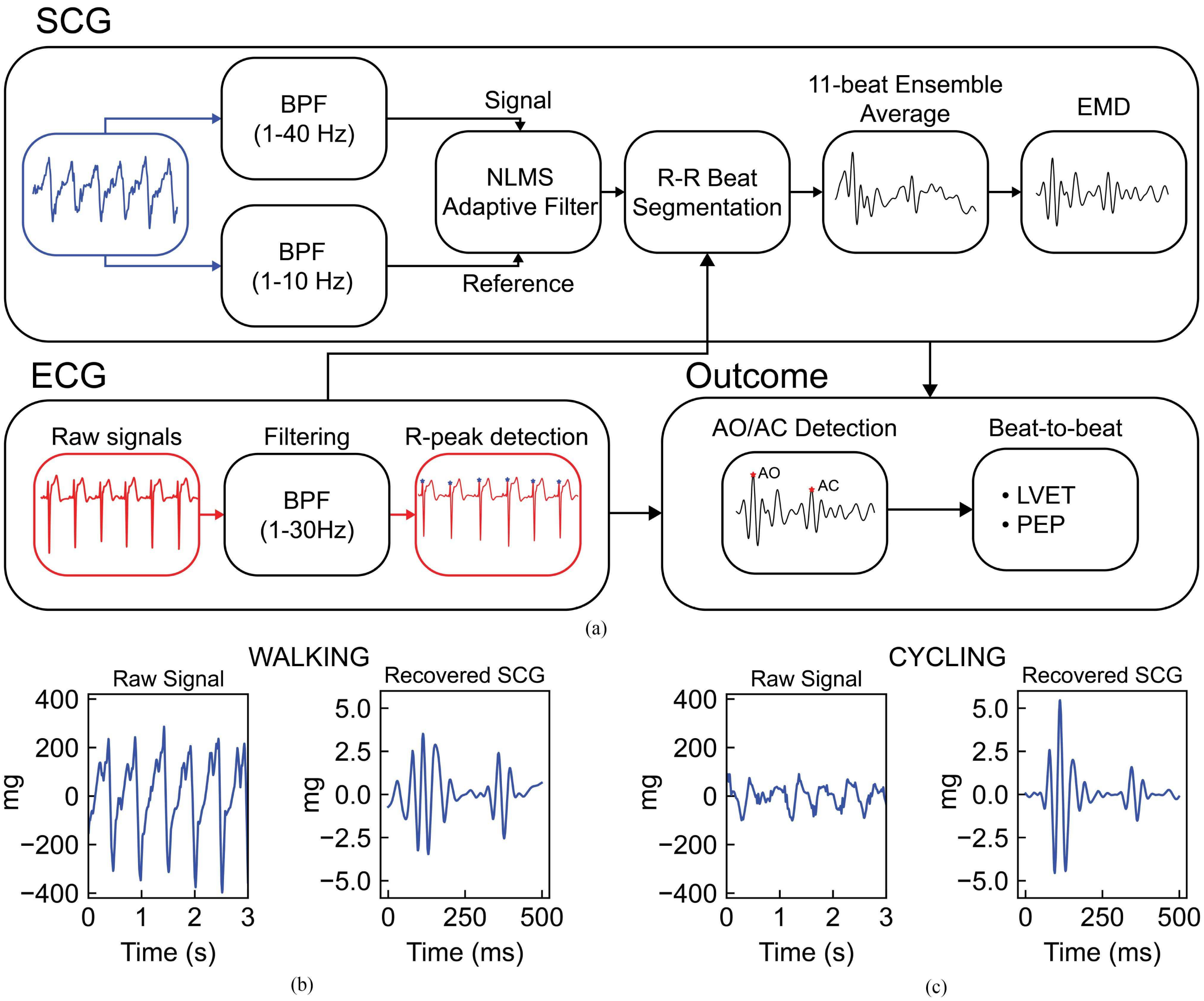

(a)

(b)

(c)

Fig. 5. (a) Block diagram of the FAD framework for both electrocardiogram (ECG) and seismocardiogram (SCG) signal processing, encompassing steps from bandpass filtering (BPF) and adaptive normalized least mean square (NLMS) filtering, to multiple beat ensemble averaging and empirical mode decomposition (EMD) for recovering the SCG signal. Extraction of the key cardiac time intervals (CTI) of interest, namely pre-ejection period (PEP) and left ventricular ejection time (LVET) is performed on the recovered signals. Results of motion compensation on SCG signals obtained through the application of the FAD framework during (b) walking and (c) cycling are shown. Plots show 3 seconds of the raw SCG signal along with a recovered heartbeat. Notably, the recovered SCG waveforms exhibit a quality comparable to that of the signal at rest.

filter with a cutoff frequency range of 1 to 10 Hz to extract the major motion component of the signal. Both signals are resampled to a sampling frequency of 1000 Hz for greater temporal resolution and then fed into the adaptive filter. The ECG signal is filtered with a bandpass filter in the range of 1 to 30 Hz and resampled similarly to 1000 Hz.

C. Motion Compensation

The FAD framework incorporates a multistage filtering approach to recover the SCG signal during motion, as illustrated in Fig. 5(a). All processing related to motion compensation was performed offline and no processing was performed on the e-tattoo or the Android device. Initially, an adaptive filter is applied, followed by beat-ensembling using the ECG R-peak as a reference. Subsequently, EMD is used and specific peaks are extracted from the first IMF. PEP and LVET are computed based on these extracted features corresponding to AO and AC.

An adaptive NLMS filter is employed to remove substantial motion artifacts from the SCG signals. The filter is implemented with a window length ‘N’ of 128 samples, a learning rate coefficient ’μ ‘ set at 0.7, and initially randomized weights. The output of the NLMS filter is segmented into individual beats using the ECG signal as a reference for segmentation. We have previously demonstrated that ECG measurements taken with dry electrodes on the e-tattoo are largely unaffected by motion interference, due to the minimized slippage at the electrode-skin interface [56]. Ensemble averaging is performed every 11 beats with an 8-beat overlap to enhance the signal-to-noise ratio (SNR), considering that the number of heartbeats required in the averaging operation is directly proportional to the walking speed [32]. Following ensemble averaging, EMD is applied to each resulting 'beat' to extract the first IMF. Subsequently, this signal is processed to extract cardiac events of interest.

D. Extraction of Key Parameters

The first IMF of each ensemble is used for the detection of AO and AC. For each activity chunk, we set the expected positions for the initial AO and AC peaks. Then, on the first IMF of the first window of ensembled beats, peaks closest to the expected positions are selected as AO and AC peaks. The positions of AO and AC peaks are then added to the arrays, and the expected positions are updated using a weighted averaging approach and used to search for peaks in the following ensemble windows.

Identified AO and AC peaks are also plotted and manually verified by a human operator. To confirm the correct positioning of the AC peak, the T wave of the ECG signal is taken as a reference. Following the peak detection process, calculations are performed to determine the PEP and LVET over time based on the detected peaks.

IV. EXPERIMENTAL RESULTS

A. Results of Motion Compensation

Fig. 5(b) provides a visual representation of both the raw signals and the results achieved in recovering the SCG signal during two distinct activities of a single participant: walking at 3 mph and cycling at 75W. 3 seconds of raw data are showcased together with a 500-ms segment of the processed signal depicting one heartbeat. In the initial raw signal captured from the participant, the presence of motion artifacts dominates, rendering the mechano-acoustic cardiac signal nearly imperceptible. However, the FAD framework exhibits remarkable efficacy in canceling out the motion-induced component of the signal, resulting in the successful recovery of the SCG beats. This achievement underscores the robustness and efficacy of our methodology in mitigating motion interference and facilitating accurate extraction of SCG data even during sustained motion.

HR obtained from the NICOM device was compared to the HR derived from the R-R interval extracted from the ECG signal captured by our e-tattoo. The resulting data demonstrated a markedly high correlation ($R = 0.997$) and precision (error $= 0.13 \pm 3.72$) in all subjects, confirming the precision of HR measurements obtained from the e-tattoo compared to a commercially available clinical device (Fig. S3). This correlation not only attests to the precision of our e-tattoo's HR measurements, but also implies that the majority of R peaks were accurately detected. This precision in the detection of the R peak is of significant importance in ensuring the correct segmentation of the beat and the correct averaging of the ensemble required for the reliable operation of the FAD framework.

In addition to HR, the NICOM device can provide LVET measurements. However, it lacks the capability to measure PEP, nor does it allow access to the raw data required for PEP extraction. Consequently, we were unable to perform a direct comparison of PEP with a gold standard measurement to assess the accuracy of the extracted PEP. However, previous research has shown a decrease in PEP with increased walking speed [29], [32]. PEP data from our e-tattoo also demonstrate this trend for all participants (Fig. S7-S9). The LVET data from NICOM can be effectively compared with the LVET calculated from the recovered SCG signal of the e-tattoo. As LVET is determined by the time interval between AO and AC, the precise detection of both events significantly contributes to the accurate measurement of LVET. In Fig. 6, we present the LVET correlation analysis between NICOM and the E-tattoo. This figure presents three representative plots, each corresponding to a different participant selected from our pool of recruited participants. These plots show a range of correlations, including the highest correlation, a low correlation, and a correlation between these extremes. Additionally, for these participants, the temporal continuity of LVET detection is illustrated, showing how LVET measurements change over time, during different activities, from both the NICOM device and our e-tattoo. For a comprehensive view of all participants' data and correlations, please refer to the supplementary materials, Figs. S4–S6.

For participants exhibiting a lower correlation in the LVET measurements between the e-tattoo and the NICOM device, a closer examination of the temporal LVET plot reveals notable deviations during the brisk walking phase. To decipher the underlying cause of this discrepancy, we construct LVET vs. HR plots for both devices, as depicted in Fig. 7. Interestingly, most of the participants demonstrated a strong negative correlation between LVET and HR when measured with e-tattoo. This agrees with the results in the literature, where LVET and HR have a negative correlation due to shorter filling times [57]. We noted that for participants with poorer LVET agreement between the e-tattoo and NICOM, the NICOM device exhibits a suspicious decrease in the correlation between its LVET and HR. Moreover, it becomes evident that during the walking phase, the LVET vs. HR plot generated by the NICOM deviates from the expected linear pattern. This observation strongly implies the challenges faced by the NICOM system in accurately extracting the LVET during motion.

As mentioned above, walking induces motion artifacts, with magnitudes nearly three times higher than those generated during cycling. Given that excessive motion interference can impact ICG measurements [58], it is plausible that the NICOM struggles to extract precise LVET data during brisk walking, thus accounting for the observed deviations in the LVET vs. HR plot.

V. DISCUSSIONS

This study addresses the significant challenge of eliminating motion artifacts in the SCG for ambulatory monitoring of CTIs. This achievement in continuous and accurate CTI monitoring during activities such as walking and cycling is made possible through both hardware and software innovations. The success in mitigating motion artifacts stems from a two-pronged strategy: first, the strategic placement of the highly flexible and conformable device to improve signal quality; and second, the implementation of a multistage processing approach. This approach named FAD includes the use of an adaptive NLMS filter, ensemble averaging, and EMD.

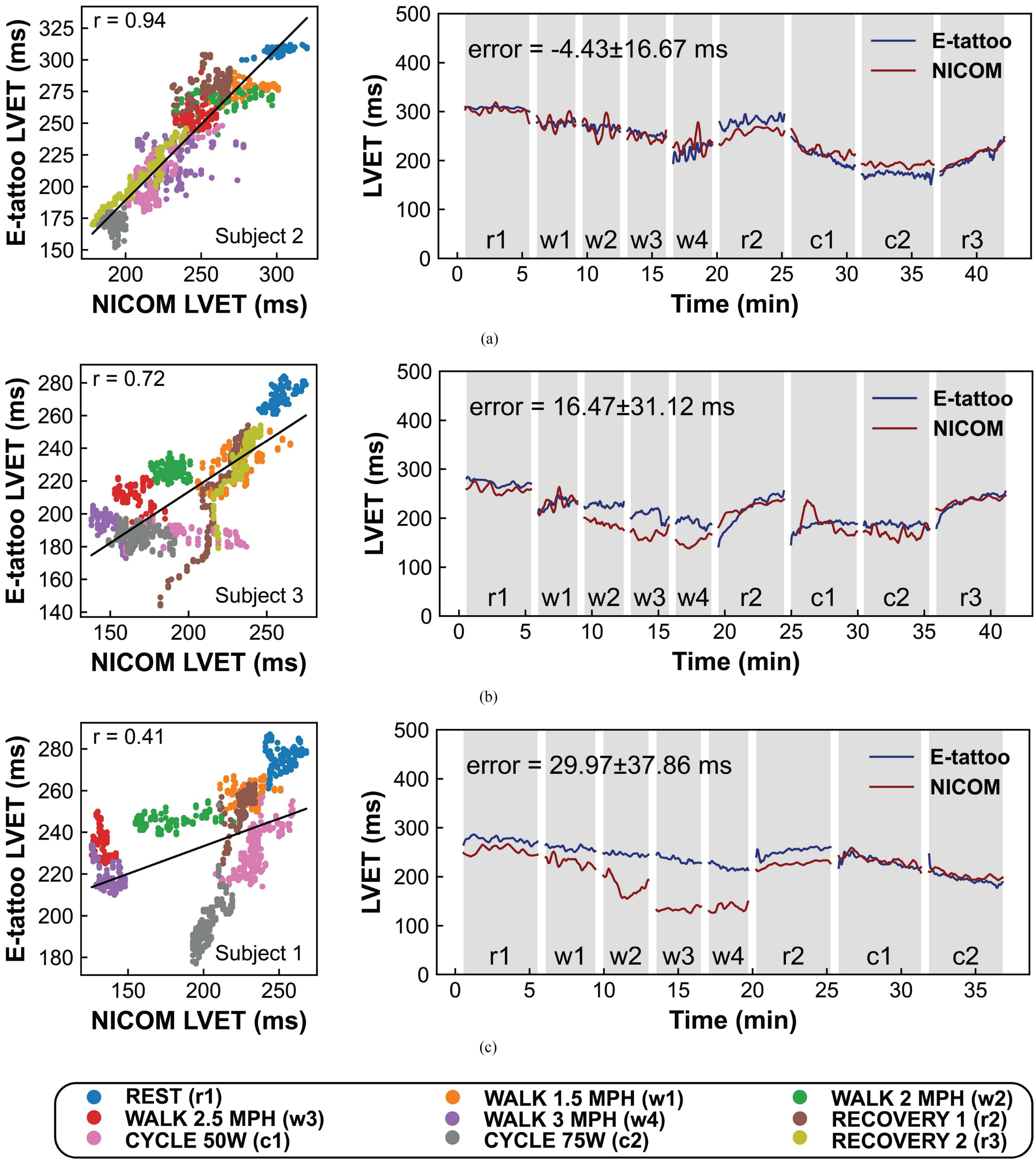

(a)

(b)

(c)

Fig. 6. Correlation plots and temporal left ventricular ejection time (LVET) profiles for three representative subjects performing designed activities. (a) Displays the subject with the highest correlation. (b) Features a subject with a moderate correlation. (c) Shows a subject with a low correlation. These correlations are drawn between LVET measurements from the e-tattoo and the NICOM device.

The strategic placement of the device contributes significantly to the success of our approach. By attaching the device to the chest, with the SCG sensor near the xiphoid process and the ECG electrodes across the sternum, we ensure optimal signal capture. Usually, the curvature of the chest in this anatomical area makes it difficult to position other rigid and bulky devices at this sensing site. The lightweight, ultrathin, and flexible form factor of our e-tattoo overcomes the positioning challenges presented by traditional rigid systems, ensuring effective SCG sensing near the heart's apex and improving signal accuracy without compromising wearer comfort during movement or long-term wear.

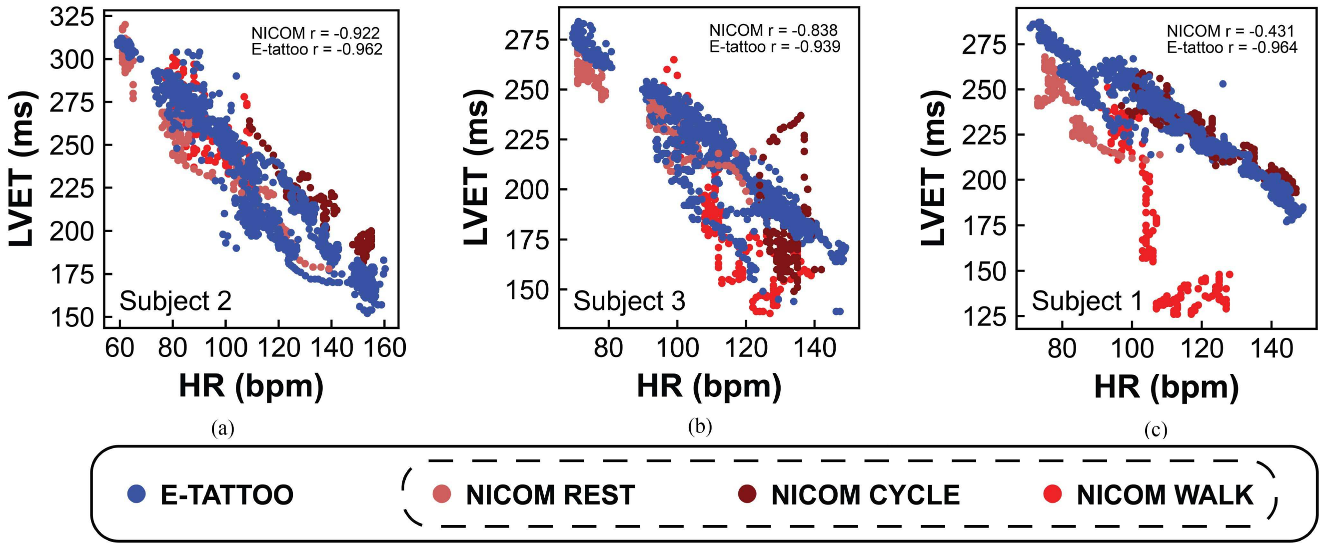

(a) (b) (c)

Fig. 7. Correlation between left ventricular ejection time (LVET) and heart rate (HR) measured by e-tattoo and NICOM for representative subjects presented in Fig. 6. As expected, a strong negative correlation is displayed. However, for Subject 1 (c), the NICOM data exhibits deviations from this expected behavior during the walking phase, indicating motion artifacts in NICOM measurements.

Within the FAD framework, the adaptive NLMS filter is designed to dynamically adjust its weights in response to large variations in the acceleration signal. This is enhanced by using ensemble averaging aligned with ECG segmentation to boost SNR and minimize beat-by-beat variability. EMD is then applied after the ensemble averaging, focusing on isolating the first IMF to refine the morphology of the SCG signal. This comprehensive and sequential noise mitigation strategy effectively isolates the SCG waveform from motion distortions, allowing a clear identification of fiducial points such as AO and AC. These points are vital for the precise calculation of CTIs such as PEP and LVET, ensuring accurate ambulatory CTI measurement in both active and at rest scenarios. We illustrate in Fig. S16 the effect of eliminating either the NMLS filter or the EMD from the framework. The results clearly show that all elements of the multistage design are required for the optimal performance of the FAD framework and the highest signal quality.

Experimental findings indicate the method's limitations at walking speeds near jogging, specifically around 4 mph, likely due to the adaptive NLMS filter's saturation at handling rapid signal changes. Such speeds intensify body movements, causing significant SCG signal fluctuations that challenge the filter's capacity to adjust dynamically, particularly affecting its ability to manage quick signal oscillations at these increased speeds.

We explored using a second coarser accelerometer as a different reference for the NMLS filter. However, because the e-tattoo had to conform to the 3D chest surface such that the two accelerometers' orientations were not perfectly aligned, there was a significant difference in the morphology of the input and reference signals, causing the framework to underperform. The results of this study are included in supplementary materials Section K.

We also explored the performance of the FAD framework on random non-periodic motion. We utilized the data that was captured when the participants were changing positions for example when getting on the treadmill or the cycle ergometer. The FAD framework successfully compensated for this range of motion as well (see Fig. S18), indicating its potential for ambulatory monitoring.

Despite its advantages, the e-tattoo hardware faces some limitations, such as the need for a hairless contact area to ensure optimal ECG signal quality and challenges with sweat tolerance. Sweat accumulation under the e-tattoo during intense activities or in warm conditions can reduce device adhesion and potentially harm exposed electronic components such as the battery. Future iterations could include a waterproof enclosure for electronics and a sweat-permeable membrane to enhance adhesion and device longevity.

At the software level, further exploration into the refinement of the adaptive NLMS filter could provide better performance during intense movements at higher speeds. Adjusting parameters like the filter's window length or learning rate, or integrating additional processing steps may enhance its effectiveness in more dynamic scenarios.

In future work, we plan to validate our hardware-software system on non-healthy populations, specifically people with cardiac disease or defects. We expect that their ECG and SCG waveform morphologies would be different from healthy subjects. It would be clinically impactful to extract continuous cardiac output or stroke volume out of the e-tattoo measureables and validate them against gold standards such as C-MRI.

VI. CONCLUSION

In conclusion, the wireless chest e-tattoo paired with the FAD framework showcases a significant leap forward in the domain of continuous ambulatory cardiac monitoring. The lightweight, ultrathin, and stretchable e-tattoo can closely adhere to the curvilinear xiphoid process area, where simultaneous high-quality ECG and SCG can be measured, for prolonged periods despite physical activities. It is supported by a comprehensive and robust algorithm for SCG noise reduction and high-accuracy CTI tracking. This innovative system can help improve the understanding of cardiovascular health through crucial CTIs such as PEP and LVET, thus significantly advancing ambulatory cardiac monitoring and facilitating the delivery of a holistic and comprehensive assessment of cardiac health.

REFERENCES

[1] A. Taebi et al., "Recent advances in seismocardiography," *Vibration*, vol. 2, no. 1, pp. 64–86, 2019.

[2] S. Sieciński, P. S. Kostka, and E. J. Tkacz, "Gyrocardiography: A review of the definition, history, waveform description, and applications," *Sensors*, vol. 20, no. 22, 2020, Art. no. 6675.

[3] F. Santucci et al., "Precordial vibrations: A review of wearable systems, signal processing techniques, and main applications," *Sensors*, vol. 22, no. 15, 2022, Art. no. 5805.

[4] M. J. Tadi et al., "Gyrocardiography: A new non-invasive approach in the study of mechanical motions of the heart. concept, method and initial observations," in *Proc. 38th Annu. Int. Conf. IEEE Eng. Med. Biol. Soc.*, 2016, pp. 2034–2037.

[5] D. L. Presti et al., "A multi-point heart rate monitoring using a soft wearable system based on fiber optic technology," *Sci. Rep.*, vol. 11, no. 1, 2021, Art. no. 21162.

[6] T. Ha et al., "A chest-laminated ultrathin and stretchable e-tattoo for the measurement of electrocardiogram, seismocardiogram, and cardiac time intervals," *Adv. Sci.*, vol. 6, no. 14, 2019, Art. no. 1900290.

[7] R. Baevskii, A. Egorov, and L. Kazarian, "The method of seismocardiography," in *Kardiologiia*, vol. 18. Chicago, IL, USA: Media Sphera, 1964, pp. 87–89.

[8] D. Salerno and J. Zanetti, "Seismocardiography a new technique for recording cardiac vibrations concept method and initial observations," *J. Cardiovasc. Technol.*, vol. 9, no. 2, pp. 111–118, 1990. [Online]. Available: https://eurekamag.com/research/007/776/007776006.php

[9] D. M. Salerno and J. Zanetti, "Seismocardiography for monitoring changes in left ventricular function during ischemia," *Chest*, vol. 100, no. 4, pp. 991–993, 1991.

[10] J. M. Zanetti, M. Poliac, and R. S. Crow, "Seismocardiography: Waveform identification and noise analysis," in *Proc. IEEE Comput. Cardiol.*, 1991, pp. 49–52.

[11] F. Perone et al., "Role of cardiovascular imaging in risk assessment: Recent advances, gaps in evidence, and future directions," *J. Clin. Med.*, vol. 12, no. 17, 2023, Art. no. 5563.

[12] D. Rai et al., "A comprehensive review on seismocardiogram: Current advancements on acquisition, annotation, and applications," *Mathematics*, vol. 9, no. 18, 2021, Art. no. 2243.

[13] G. Cosoli et al., "Wireless ecg and cardiac monitoring systems: State of the art, available commercial devices and useful electronic components," *Measurement*, vol. 177, 2021, Art. no. 109243.

[14] D. M. Salerno et al., "Seismocardiographic changes associated with obstruction of coronary blood flow during balloon angioplasty," *Amer. J. Cardiol.*, vol. 68, no. 2, pp. 201–207, 1991.

[15] K. Tavakolian et al., "Myocardial contractility: A seismocardiography approach," in *Proc. IEEE Annu. Int. Conf. IEEE Eng. Med. Biol. Soc.*, 2012, pp. 3801–3804.

[16] W.-Y. Lin et al., "Identification of location specific feature points in a cardiac cycle using a novel seismocardiogram spectrum system," *IEEE J. Biomed. Health Inform.*, vol. 22, no. 2, pp. 442–449, Mar. 2016.

[17] K. Tavakolian et al., "Estimation of hemodynamic parameters from seismocardiogram," in *2010 IEEE Comput. Cardiol.*, 2010, pp. 1055–1058.

[18] S. Ismail, I. Siddiqi, and U. Akram, "Localization and classification of heart beats in phonocardiography signals—a comprehensive review," *EURASIP J. Adv. Signal Process.*, vol. 2018, no. 1, pp. 1–27, 2018.

[19] W. Yan et al., "Single fibre enables acoustic fabrics via nanometre-scale vibrations," *Nature*, vol. 603, no. 7902, pp. 616–623, 2022.

[20] K. Sørensen et al., "Author correction: Definition of fiducial points in the normal seismocardiogram," *Sci. Rep.*, vol. 10, no. 1, 2020, Art. no. 14822.

[21] Z. Xia et al., "The delineation of fiducial points for non-contact radar seismocardiogram signals without concurrent ECG," *IEEE J. Biomed. Health Informat.*, vol. 25, no. 4, pp. 1031–1040, Apr. 2021.

[22] T. Biering-Sørensen et al., "Cardiac time intervals measured by tissue Doppler imaging m-mode: Association with hypertension, left ventricular geometry, and future ischemic cardiovascular diseases," *J. Amer. Heart Assoc.*, vol. 5, no. 1, 2016, Art. no. e002687.

[23] C. L. Garrard Jr, A. M. Weissler, and H. T. Dodge, "The relationship of alterations in systolic time intervals to ejection fraction in patients with cardiac disease," *Circulation*, vol. 42, no. 3, pp. 455–462, 1970.

[24] A. S. Alhakak et al., "The significance of left ventricular ejection time in heart failure with reduced ejection fraction," *Eur. J. Heart Failure*, vol. 23, no. 4, pp. 541–551, 2021.

[25] A. S. Alhakak et al., "Left ventricular systolic ejection time is an independent predictor of all-cause mortality in heart failure with reduced ejection fraction," *Eur. J. Heart Failure*, vol. 23, no. 2, pp. 240–249, 2021.

[26] K. Pandia et al., "Motion artifact cancellation to obtain heart sounds from a single chest-worn accelerometer," in *Proc. IEEE Int. Conf. Acoust., Speech Signal Process.*, 2010, pp. 590–593.

[27] C. Yang and N. Tavassolian, "Motion artifact cancellation of seismocardiographic recording from moving subjects," *IEEE Sensors J.*, vol. 16, no. 14, pp. 5702–5708, Jul. 2016.

[28] C. Yang and N. Tavassolian, "Motion noise cancellation in seismocardiogram of ambulant subjects with dual sensors," in *2016 38th Annu. Int. Conf. IEEE Eng. Med. Biol. Soc.*, 2016, pp. 5881–5884.

[29] C. Yang and N. Tavassolian, "An independent component analysis approach to motion noise cancelation of cardio-mechanical signals," *IEEE Trans. Biomed. Eng.*, vol. 66, no. 3, pp. 784–793, Mar. 2019.

[30] H. Lee and M. Whang, "Heart rate estimated from body movements at six degrees of freedom by convolutional neural networks," *Sensors*, vol. 18, no. 5, Art. no. 1392, 2018.

[31] S. Yu and S. Liu, "A novel adaptive recursive least squares filter to remove the motion artifact in seismocardiography," *Sensors*, vol. 20, no. 6, 2020, Art. no. 1596.

[32] A. Q. Javaid et al., "Quantifying and reducing motion artifacts in wearable seismocardiogram measurements during walking to assess left ventricular health," *IEEE Trans. Biomed. Eng.*, vol. 64, no. 6, pp. 1277–1286, Jun. 2017.

[33] R. Khusainov et al., "Real-time human ambulation, activity, and physiological monitoring: Taxonomy of issues, techniques, applications, challenges and limitations," *Sensors*, vol. 13, no. 10, pp. 12852–12902, 2013.

[34] J. M. Hausdorff et al., "When human walking becomes random walking: Fractal analysis and modeling of gait rhythm fluctuations," *Physica A: Stat. Mech. Its Appl.*, vol. 302, no. 1-4, pp. 138–147, 2001.

[35] A. M. Weissler, J. J. Leonard, and J. V. Warren, "Observations on the delayed first heart sound in mitral stenosis and hypertension," *Circulation*, vol. 18, no. 2, pp. 165–168, 1958.

[36] A. Dodek, J. R. Burg, and F. E. Kloster, "Systolic time intervals in chronic hypertension: Alterations and response to treatment," *Chest*, vol. 68, no. 1, pp. 51–55, 1975.

[37] H. Boudoulas et al., "Systolic time intervals in atrial fibrillation," *Chest*, vol. 74, no. 6, pp. 629–634, 1978.

[38] S. Bhattacharya et al., "A chest-conformable, wireless electro-mechanical e-tattoo for measuring multiple cardiac time intervals," *Adv. Electron. Mater.*, vol. 9, no. 9, 2023, Art. no. 2201284.

[39] N. Lu and S. Yang, "Mechanics for stretchable sensors," *Curr. Opin. Solid State Mater. Sci.*, vol. 19, no. 3, pp. 149–159, 2015.

[40] N. Meziane et al., "Dry electrodes for electrocardiography," *Physiol. Meas.*, vol. 34, no. 9, 2013, Art. no. R47.

[41] A. A. Chlaihawi et al., "Development of printed and flexible dry ecg electrodes," *Sens. Bio-Sensing Res.*, vol. 20, pp. 9–15, 2018.

[42] R. Fadil et al., "Temporal changes of fiducial seismocardiogram points due to different sensor placements on the chest," in *Proc. IEEE Comput. Cardiol.*, 2020, pp. 1–4.

[43] D. Sadhukhan et al., "Morphological and temporal variations of seismocardiograms across the chest: A guide for single channel sensor placement," in *2023 IEEE Comput. Cardiol.*, 2023, vol. 50, pp. 1–4.

[44] F. Santucci et al., "Waveform similarity analysis using graph mining for the optimization of sensor positioning in wearable seismocardiography," *IEEE Trans. Biomed. Eng.*, vol. 70, no. 10, pp. 2788–2798, Oct. 2023.

[45] M. K. Azad et al., "Spatial distribution of seismocardiographic signals," *Biomed. Signal Process.: Innov. Appl.*, 2021, pp. 129–159.

[46] K. Munck et al., “Multichannel seismocardiography: An imaging modality for investigating heart vibrations,” *Physiol. Meas.*, vol. 41, no. 11, 2020, Art. no. 115001.

[47] C. Romano et al., “Investigation of body locations for cardiac and respiratory monitoring with skin-interfaced inertial measurement unit sensors,” *IEEE Sensors J.*, vol. 23, no. 7, pp. 7806–7815, Apr. 2023.

[48] A. Mann et al., “Exploring the impact of sensor location on seismocardiography-derived cardiac time intervals,” *J. Eng. Sci. Med. Diagnostics Ther.*, vol. 7, no. 1, pp. 1–19, 2024.

[49] R. Martinek et al., “A phonocardiographic-based fiber-optic sensor and adaptive filtering system for noninvasive continuous fetal heart rate monitoring,” *Sensors*, vol. 17, no. 4, 2017, Art. no. 890.

[50] R. S. A. Araújo et al., “Analysis of adaptive algorithms based on least mean square applied to hand tremor suppression control,” *Appl. Sci.*, vol. 13, no. 5, 2023, Art. no. 3199.

[51] Y. S. Lee et al., “Physics-based foundation for empirical mode decomposition,” *AIAA J.*, vol. 47, no. 12, pp. 2938–2963, 2009.

[52] N. E. Huang et al., “The empirical mode decomposition and the Hilbert spectrum for nonlinear and non-stationary time series analysis,” *Proc. Roy. Soc. London Ser. A: Math., Phys. Eng. Sci.*, vol. 454, no. 1971, pp. 903–995, 1998.

[53] Z. Wu and N. E. Huang, “On the filtering properties of the empirical mode decomposition,” *Adv. Adaptive Data Anal.*, vol. 2, no. 04, pp. 397–414, 2010.

[54] N. E. Huang, “New method for nonlinear and nonstationary time series analysis: Empirical mode decomposition and Hilbert spectral analysis,” *Proc. SPIE*, vol. 4056, pp. 197–209, 2000.

[55] D. Labate et al., “Empirical mode decomposition vs. wavelet decomposition for the extraction of respiratory signal from single-channel ECG: A comparison,” *IEEE Sensors J.*, vol. 13, no. 7, pp. 2666–2674, Jul. 2013.

[56] Y. Wang et al., “Low-cost, μm-thick, tape-free electronic tattoo sensors with minimized motion and sweat artifacts,” *npj Flexible Electron.*, vol. 2, no. 1, 2018, Art. no. 6.

[57] A. M. Weissler, W. S. Harris, and C. D. Schoenfeld, “Systolic time intervals in heart failure in man,” *Circulation*, vol. 37, no. 2, pp. 149–159, 1968.

[58] A. Sherwood et al., “Methodological guidelines for impedance cardiography,” *Psychophysiology*, vol. 27, no. 1, pp. 1–23, 1990.